High-Pressure Mg_3Cl_7 Synthesized in a Diamond Anvil Cell as a Polar Metal with Second-Harmonic Generation

Article *in* Journal of the American Chemical Society · September 2025

DOI: 10.1021/jacs.5c07812

High-Pressure Mg_3Cl_7 Synthesized in a Diamond Anvil Cell as a Polar Metal with Second-Harmonic Generation

Yuqing Yin[1,2*], Leonid Dubrovinsky[3*], Ferenc Tasnádi[2], Igor A. Abrikosov[2], Andrey Aslandukov[4], Alena Aslandukova[4], Fariia Iasmin Akbar[4], Wenju Zhou[1,3], Florian Knoop[2], Dominique Laniel[5], Anna Pakhomova[6], Timofey Fedotenko[7], Konstantin Glazyrin[7], Gaston Garbarino[6], Haixing Fang[6], Natalia Dubrovinskaia[1,2]

Affiliations:

[1]Material Physics and Technology at Extreme Conditions, Laboratory of Crystallography, University of Bayreuth, 95440 Bayreuth, Germany
[2]Department of Physics, Chemistry and Biology (IFM), Linköping University, SE-581 83, Linköping, Sweden
[3]Bayerisches Geoinstitut, University of Bayreuth, 95440 Bayreuth, Germany
[4]Institute of Inorganic and Analytical Chemistry, Goethe University Frankfurt, Max-von-Laue-Straße 7, 60438 Frankfurt, Germany
[5]Centre for Science at Extreme Conditions and School of Physics and Astronomy, University of Edinburgh, EH9 3FD Edinburgh, United Kingdom
[6]European Synchrotron Radiation Facility, 38000 Grenoble, France
[7]Deutsches Elektronen-Synchrotron DESY, Notkestr. 85, 22607 Hamburg, Germany
*Corresponding authors. Email: Yuqing.Yin@uni-bayreuth.de; Leonid.Dubrovinsky@uni-bayreuth.de

Abstract: Polar metals have attracted growing interest due to their significance in both fundamental science and potential functionalities. Here, we report the discovery of a novel polar metal, magnesium chloride Mg_3Cl_7, in which the metallicity of the polar structure is uniquely driven by attractive halogen interactions. Mg_3Cl_7 was synthesized in laser-heated diamond anvil cells and observed at pressures of 28(2)-93(3) GPa. Synchrotron single-crystal X-ray diffraction revealed that the structure of the new compound has the polar hexagonal space group $P6_3mc$, representing an example of a previously unknown *anti*-Th_7Fe_3 structure type. Measurements of the physical properties have shown that the material is a metallic conductor capable of emitting second-harmonic generation light. *Ab initio* calculations support experimental findings and reveal complex halogen-halogen interactions, anionic metallicity, anisotropic electronic structure, and the presence of Dirac and Weyl points at the Fermi level. Our findings broaden the family of polar metals, provide new insight into halogen bonding under extreme conditions, and offer a platform for further exploration of materials' unconventional electronic behavior.

1. Introduction

Polar metals represent an intriguing class of materials where polarity and metallicity coexist in the same phase, which may seem counterintuitive due to the screening effect of free carriers on long-range dipole-dipole interactions.[1] Anderson and Blount first proposed theoretically in 1965 a route how polar metals could be synthesized deliberately through a second-order transition of a metallic phase, that might be accompanied by the appearance of a polar axis.[2] Its experimental validation occurred in 2013 when Shi *et al.* reported a ferroelectric-like (FE-like) structural transition in the metallic perovskite $LiOsO_3$.[3] This transition involves symmetry lowering from the centrosymmetric space group $R\bar{3}c$ to non-centrosymmetric $R3c$ upon cooling below 140 K.[3] The unique interplay of polarity and metallicity provides an opportunity to study unusual physical phenomena, which has led to increased research interest over the past decade.[4-9]

Despite notable progress, the experimental synthesis of new polar metals remains a considerable challenge, and much remains to be learned about mechanisms of polar distortion in metallic materials.[10] High-pressure (HP) synthesis provides an opportunity for modifying chemical bonding and stabilizing unconventional phases. Recent studies have demonstrated that halogen bonding under HP can be stabilized with the formation of polyhalogen anions with partially filled *p*-bands crossing the Fermi level, thereby contributing to metallic conductivity. Examples include the *cP*8-AX_3 (A = Na, K, Cs, and X = Cl, Br, I) and the Na_4X_5 (X = Cl and Br) compounds,[11-12] where pressure-driven bonding rearrangements and electron delocalization enable the anionic metallic properties. To date, however, there are no experimental works on synthesis and structural characterization of high-pressure halogenides of main second group elements. For this reason, we selected the Mg-Cl system as a natural object to start with.

Non-homoatomic halogen compounds are characterized by polar covalent/ionic bonding between halogen and non-halogen atoms. This bonding leads to an asymmetric electron distribution, resulting in a region of higher electron density, where the electrostatic potential is negative, forming an electron-rich belt perpendicular to the covalent bond. At the bond extension along the halogen atom's σ-axis, a region of depleted electron density, known as a σ-hole, appears. This σ-hole is associated with a localized region of positive electrostatic potential, facilitating non-covalent interactions such as halogen bonding. Such an anisotropic charge distribution around halogen atoms can induce molecular or structural polarity in crystals containing these elements, which is crucial for obtaining non-centrosymmetric structures.[13] These effects are expected to become particularly significant under high pressure, where the interplay between pressure-induced (or pressure-stabilized) polyhalogen anions and the inherent asymmetry of halogen-involved polar covalent bonding provides a pathway for the synthesis of novel polar (anionic) metals. This, in turn, enables the coexistence of polarity and metallicity—an effect driven by halogen bonding that is difficult to achieve under ambient conditions.

Here, using single-crystal X-ray diffraction (SCXRD) as a tool for the chemical and phase composition determination, and structural characterization of the materials,[14] we have studied products of chemical reactions in the Mg-Cl system at pressures up to 93 GPa in laser-heated diamond anvil cells (LHDACs). Among others, the Mg_3Cl_7 compound was found to have a number of interesting properties revealed both experimentally and computationally. Its structure has the polar space group $P6_3mc$ that agrees well with the experimental observation of the second-harmonic generation in this material. Temperature-dependent electrical resistance measurements and *ab initio* calculations confirm the metallic nature of the Mg_3Cl_7 compound. Density functional theory (DFT) calculations shed light on the complex halogen bonding and electronic properties of the novel compound.

2. Sample preparation and experimental procedure

Two DACs were prepared to study the behavior of Mg-Cl system in a wide pressure range (see Methods below). Both DACs were loaded with magnesium and carbon tetrachloride (Mg + CCl_4). For DAC #1, SCXRD data were collected on quenched samples after laser heating (LH) at several pressures from 44(3) to 83(3) GPa. The samples were then decompressed and the SCXRD data were collected at 28(2) and 7(2) GPa after a second LH (Table S1). In addition to the Mg_3Cl_7 compound found at all pressure points between 28(2) and 83(3) GPa, the data at pressures ~7 to ~83 GPa also revealed three different polymorphs of magnesium dichloride (β-$MgCl_2$[15], *oP*72-$MgCl_2$, and *oP*12-$MgCl_2$), which will be described and discussed elsewhere. DAC #2 was prepared using the same starting materials (Mg + CCl_4), but flakes of magnesium foil were connected to Pt electrodes outside the pressure chamber in order to perform resistance measurements after LH of the sample. For DAC #2 SCXRD data were collected at 65(5) and 93(3) GPa (Table S1). In addition to the successfully reproduced synthesis of Mg_3Cl_7, a small amount of an impurity, magnesium hydroxychloride Mg(OH)Cl, was detected in DAC #2. This impurity likely resulted from increased air exposure of Mg while placing the electrodes. A detailed discussion on the crystal structure and calculated insulating property of Mg(OH)Cl are provided in Supplementary Discussion 1.

3. Results

3.1 Experimental

3.1.1 Crystal Structure and Second-Harmonic Generation

The structure of magnesium chloride, Mg_3Cl_7, has the polar hexagonal space group $P6_3mc$ (#186), as solved and refined from high quality synchrotron SCXRD data. Examples of the reconstructed reciprocal lattice planes are shown in Fig. S1. All observed reflections can be indexed within the $P6_3mc$ symmetry, and no reflections that violate the X-ray extinction rules were detected. At the synthesis pressure of 44(3) GPa, the lattice parameters are a=7.936(2) Å and c=4.995(3) Å (see the structure model in Fig. 1, refinement details are provided in Table S2, CIFs deposited under CSD 2448699-2448705). Mg atoms occupy the 6*c* Wyckoff site, and Cl1, Cl2, and Cl3 atoms are in the Wyckoff sites 2*b*, 6*c*, and 6*c*, respectively. Each Mg atom is coordinated by six Cl atoms, forming a distorted trigonal prism. Three $MgCl_6$ prisms form triads, as each prism shares two edges of one of its triangular bases with two other prisms, so that the common edges "meet" at atom Cl1 (shown in green in Fig. 1) forming a triangular pyramid with the base of three Cl3 atoms (shown in blue in Fig. 1). These triads stack one upon another along the 3-fold rotation axes, forming layers of triads in the *ab* plane. The triads, both within the layers and between the neighbouring layers, are interconnected through sharing vertices of the second triangular base of each of the prisms (Fig. 1a,b), formed by atoms Cl2 (shown in cyan in Fig. 1). Coordination of Cl atoms with respect to Mg is highlighted in Fig. 1c. The structure of Mg_3Cl_7 can be described as an anti-Th_7Fe_3-type.

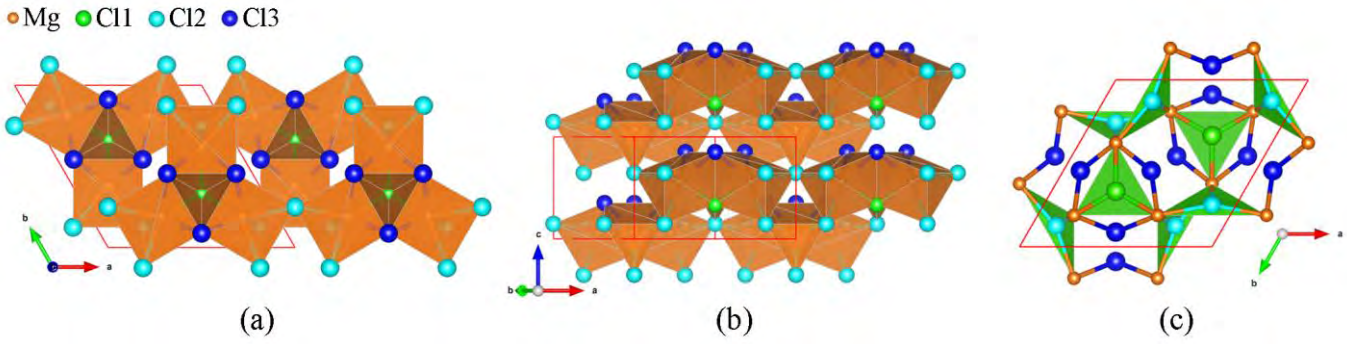

Fig. 1. The structure of the novel magnesium chloride Mg_3Cl_7 synthesized in this work. (a) Polyhedral model in $MgCl_6$ polyhedra (brown) as viewed along the *c* direction; the unit cell is outlined in red; (b) a view of the structure perpendicular to *c* direction, highlighting the stacking of the triads, built of triangular

prisms, along the *c* direction;(c) a view along the *c* direction highlighting the coordination of Cl atoms with respect to magnesium; Mg atoms are orange, Cl1 atoms are green (coordination number on Mg, CN=3), Cl2 atoms are cyan (CN=3), Cl3 atoms are blue (CN=2).

Decompression experiments were carried out for DAC #1. The sample was decompressed from 83(3) GPa to 28(2) GPa and laser heated; Mg_3Cl_7 could still be detected using SCXRD (Table S2). The second step of decompression was down to ~15 GPa. However, during the LH at this pressure, that is required for recrystallization of the material for obtaining good-quality SCXRD data, the pressure dropped further down to 7(2) GPa, at which only β-$MgCl_2$[15] was detected.

Material(s) produced by the chemical reaction of Mg and CCl_4 in our experiments at each pressure point during laser heating demonstrate second harmonic generation (SHG), as they produce green light (536 nm) (Fig. 2) being illuminated by a near-infrared (NIR) laser (1070(2) nm wavelength). SHG is a second-order non-linear optical process, which causes the frequency doubling of the light and is strictly forbidden in centrosymmetric structures. Therefore, its observation in laser-heated DACs (see Methods) provides direct proof of non-centrosymmetric structure of the synthesized phases. Considering that among the reaction products only Mg_3Cl_7 is non-centrosymmetric (the $MgCl_2$ and Mg(OH)Cl compounds both have centrosymmetric structures (see Supplementary Discussions 1), the SHG signal can solely be attributed to Mg_3Cl_7. The SHG signal was clearly observed in independent synthesis experiments at each pressure point, demonstrating the reproducibility of the optical response under high-pressure conditions. We emphasize that the SHG intensity measured under HP conditions from laser heated multicrystalline samples is affected by uncontrolled factors such as crystalline quality (polycrystallinity, defects, twinning, stresses, disorder, etc.), orientation of crystal (or crystallites), quality of the crystal/crystallites surface, sample thickness, etc. Therefore, the observed signal is interpreted as qualitative evidence of polarity rather than a quantitative measure of non-linear optical effects.

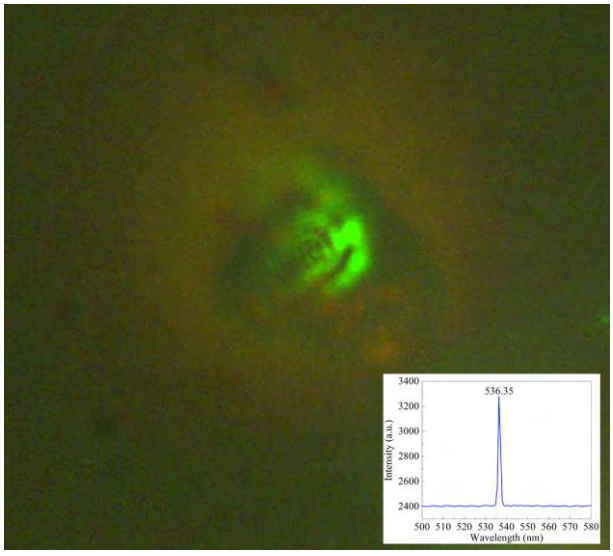

Fig. 2. Microphotograph of the pressure chamber of DAC #1 during laser heating. Green-colored light is produced when irradiating the sample with the NIR laser (λ = 1070(2) nm). This is attributed to the non-linear optical properties of the formed compound, Mg_3Cl_7, producing photons of wavelength corresponding to the green color, through second-order harmonic generation. Inset is the collected SHG signal under excitation wavelength of 1070(2) nm.

3.1.2 Electrical Resistance

The metallic behavior of Mg_3Cl_7 was confirmed experimentally by measuring its resistance in DAC #2 (see Methods). The resistance showed linear dependence on temperature and increased with increasing temperature that is typical for metals (Fig. 3). The resistance of Pt measured in similar PT conditions in DAC #3 showed metallic behavior that justified the validity of the results for Mg_3Cl_7, which can be considered solely as qualitative. The following factors were considered to ensure that the microstructural heterogeneity (see inset in Fig. 3) did not affect the electrical transport measurements. Before LH of the magnesium flake in the DAC, the resistance of the sample was ~0.05 Ω, but it significantly increased to ~0.18 Ω, as measured at 298 K after LH that gives evidence that it is rather due to the change of the sample composition than due to the current leakage or short-circuiting through Mg metal. The former is confirmed by the XRD map (see inset in Fig. 3), which provides information about phase composition of the sample. The larger blue-colored area in the XRD map corresponds to Mg_3Cl_7, and a small yellow-colored – to a tiny impurity of Mg(OH)Cl. The latter is predicted to be insulating based on our DFT calculations (see Supplementary Discussion 1). Thus, the resistance changes with temperature typical for metals is due to intrinsic behavior of Mg_3Cl_7.

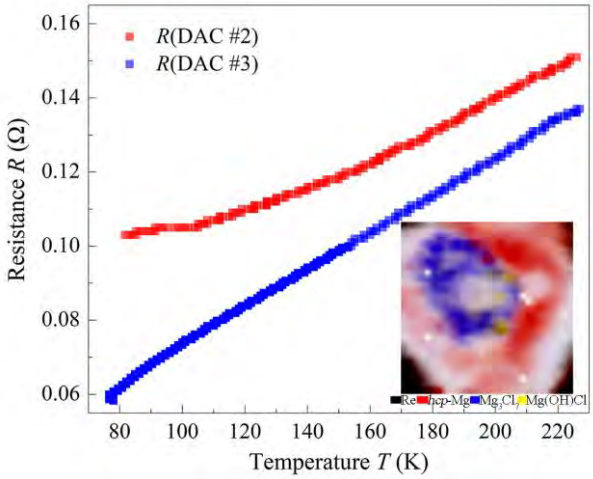

Fig. 3. The resistance of Mg_3Cl_7 (measured in DAC #2 at 65(5) GPa; red points) and Pt (measured in DAC #3 at 65(2) GPa; blue points) as functions of temperature. The inset is the XRD map of the pressure chamber of DAC #2 at 65(5) GPa, showing distribution of phases in the measured sample: *hcp*-Mg (red), served for connecting electrodes for the resistance measurements; Mg_3Cl_7 (blue), and Mg(OH)Cl (yellow); areas seen as white-coloured are due to CCl_4. Black color outlines the boundary of the Re gasket holding the pressure chamber.

3.2 Theoretical

3.2.1 Structural Relaxation, Stability, and the Equation of State of Mg_3Cl_7

Our DFT calculations with the PBE + optB88 functional reproduced the crystal structure of the Mg_3Cl_7 compound in good agreement with the experimental data (Fig. 4, Tables S2). For example, for the volume fixed at the experimental value of ~272.4 $Å^3$ at 44(3) GPa, the calculations give the pressure of 42 GPa; the relaxed unit cell parameters closely reproduce the corresponding experimental values (Table S2). Concerning the interatomic distances, PBE + optB88 calculations are in good agreement with the experimental Mg-Cl and Cl-Cl distances overall but underestimate the Cl1-Cl3 distances. For example, at ~44 GPa, the experimental average Mg-Cl bond length in a $MgCl_6$ prism is 2.31 Å that is very close to the calculated value of 2.33 Å, and for the Cl3-Cl3 distance the difference is very small (experimental 2.78 Å vs theoretical 2.74 Å), whereas for the Cl1-Cl3 distance there is a slightly larger difference of 0.12 Å (experimental 2.96 Å vs theoretical 2.84 Å, about 4% difference).

Convex hulls for Mg-Cl system were constrained at 0, 50, and 100 GPa considering *hcp*- or *bcc*-Mg, *oC*8-Cl, known $MgCl_2$ phases, and Mg_3Cl_7 phase. We found that the corresponding points of Mg_3Cl_7 are located above the static convex hull simulated at 0 K (Fig. 4a), with values of 97.7, 25.8, and 50.4 meV/atom at 0, 50, and 100 GPa, respectively. The latter two values are well below the "standard" 70 meV/atom limit for metastability,[16] and all values are smaller than the thermal energy contribution of ~184 meV/atom (k_BT at ~2200 K).

Full variable-cell structure relaxations of Mg_3Cl_7 were performed with 10 GPa pressure steps in the range of 0-100 GPa. DFT calculations suggest that the $MgCl_6$ prisms transform into octahedrally coordinated Mg at 1 bar (Fig. S2a). Phonon dispersion curves for Mg_3Cl_7 at both high pressure of ~42 GPa (experimental volume of ~272.4 Å^3) and 1 bar are shown in Fig. 4b and Fig. S2b. Little imaginary frequency (0.05 THz) is presented in the vicinity of the Γ point over the whole Brillouin zone, which is due to numerical effect. Therefore, it can be concluded that the Mg_3Cl_7 compound is dynamically stable at both ~42 GPa and 1 bar.

The pressure dependence of the volume per atom for Mg_3Cl_7 (based on the pressure-volume relations from our DFT calculations) is shown in Fig. 4c, along with the experimental data points. The measured experimental volumes from SCXRD match well with the theoretical calculations. The bulk modulus of Mg_3Cl_7 of $K_0 = 32(3)$ GPa (with V_0 = 21.3(3) Å^3/atom, K' = 4.70(15)) was determined from the third-order Birch-Murnaghan equation of state.

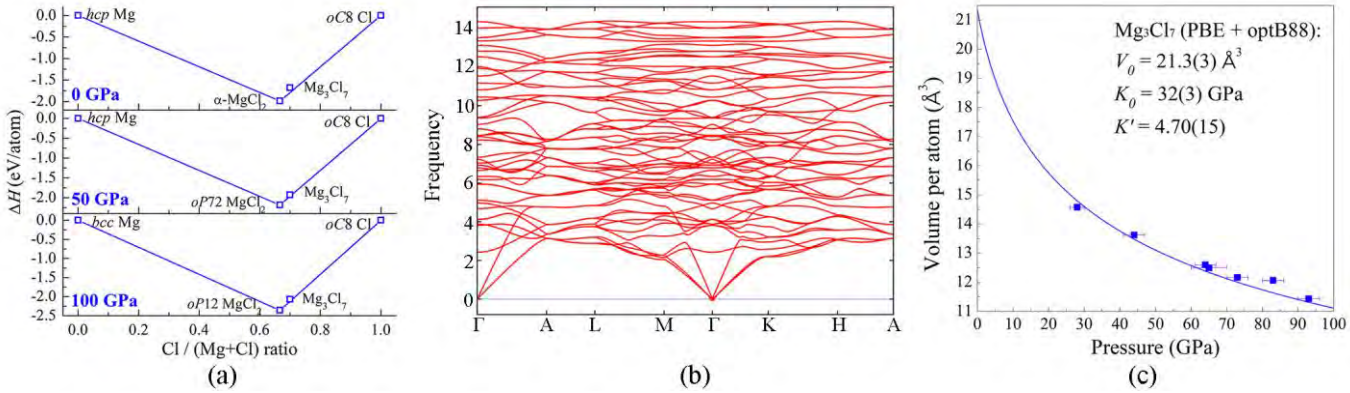

Fig. 4. The results of theoretical calculations with the PBE + optB88 functional. (a) Convex hull diagram for the Mg-Cl system at different pressures. For each composition, only the phase with the lowest enthalpy is shown (*hcp*-Mg at 0, 50 GPa, and *bcc*-Mg at 100 GPa;[17] *oC*8-Cl from 0 to 100 GPa;[18] α-$MgCl_2$ from 0 to 0.7 GPa,[15] β-$MgCl_2$ from 0.7 to 49 GPa, *oP*72-$MgCl_2$ from 49 to 52 GPa, and *oP*12-$MgCl_2$ from 52 to 100 GPa). (b) Phonon dispersion curves of Mg_3Cl_7 calculated along high-symmetry directions in the Brillouin zone at ~42 GPa (experimental volume of ~272.4 Å^3). (c) The pressure dependence of the volume per atom based on the pressure-volume relations from our DFT calculations in comparison with experimental data for Mg_3Cl_7. Blue line represents the fit of the pressure-volume data (volume was DFT-calculated for given pressures) by the third-order Birch-Murnaghan equation of state (K_0 = 32(3) GPa, V_0 = 21.3(3) Å^3/atom, K' = 4.70(15)). Blue squares represent experimental values.

3.2.2. Electronic Properties of Mg_3Cl_7

The metallicity of the polar Mg_3Cl_7 compound was revealed not only experimentally, but also by DFT calculations using both GGA (PBE) (Fig. 5) and hybrid (HSE06) (Fig. S3) functionals. According to the band structure and the total and projected density of states (TDOS and PDOS) curves, Mg_3Cl_7 exhibits metallic properties at ~40 GPa, with few bands of the Cl-*p* states ($3p_x$, $3p_y$, and $3p_z$) crossing the Fermi energy E_F. The metallicity of Mg_3Cl_7 is thus solely due to the contribution from anions (the Cl-3*p* orbitals, primarily $3p_z$), suggesting that Mg_3Cl_7 is an anionic metal. The phenomenon was previously reported for high-pressure di- and poly-nitrides.[19-20] It is worth to note that the TDOS and band structures (Fig. 5a,b) of Mg_3Cl_7 show

similarities to those of heavily doped semiconductors. For example, in the case of the defect-controlled hole doping in $MgCl_2$ layers,[21] a creation of the holes shifts the Fermi level lower inside the valence band. Although Mg_3Cl_7 is a stoichiometric compound without any deliberate addition of dopants, its electronic structure exhibits similarities to such systems.

A detailed analysis of the band structure of Mg_3Cl_7 (Fig. 5b) reveals a steep energy dispersion along the **Γ-A** direction in the Brillouin zone, coupled with a Dirac cone band touching at the **K** point. This suggests highly delocalized electronic states and robust directional bonding interactions along the *c*-axis, promoting anisotropic conductivity and overlap between the interaction orbitals. Theoretical studies have suggested that some LiGaGe-type hexagonal non-centrosymmetric Dirac semimetals can host coexisting Dirac and Weyl points,[22] which is unusual. Interestingly, the calculated Fermi surface of Mg_3Cl_7 (Fig. 5c) indicates similar features, with isolated point touching of two bands occurring at the energy $E - E_F = +0.18$ eV, giving rise to a topological Weyl point (Fig. 5d, highlighted by the yellow arrow; see detailed analysis of the electronic band topology of Mg_3Cl_7 in Supplementary Discussion 2). Additionally, plasmon frequency calculations further reveal significant directional dependence in collective electron oscillations, with values of 1.267 eV in the *a* and *b* directions, and in contrast, a significantly higher value of 2.274 eV along the *c* direction.

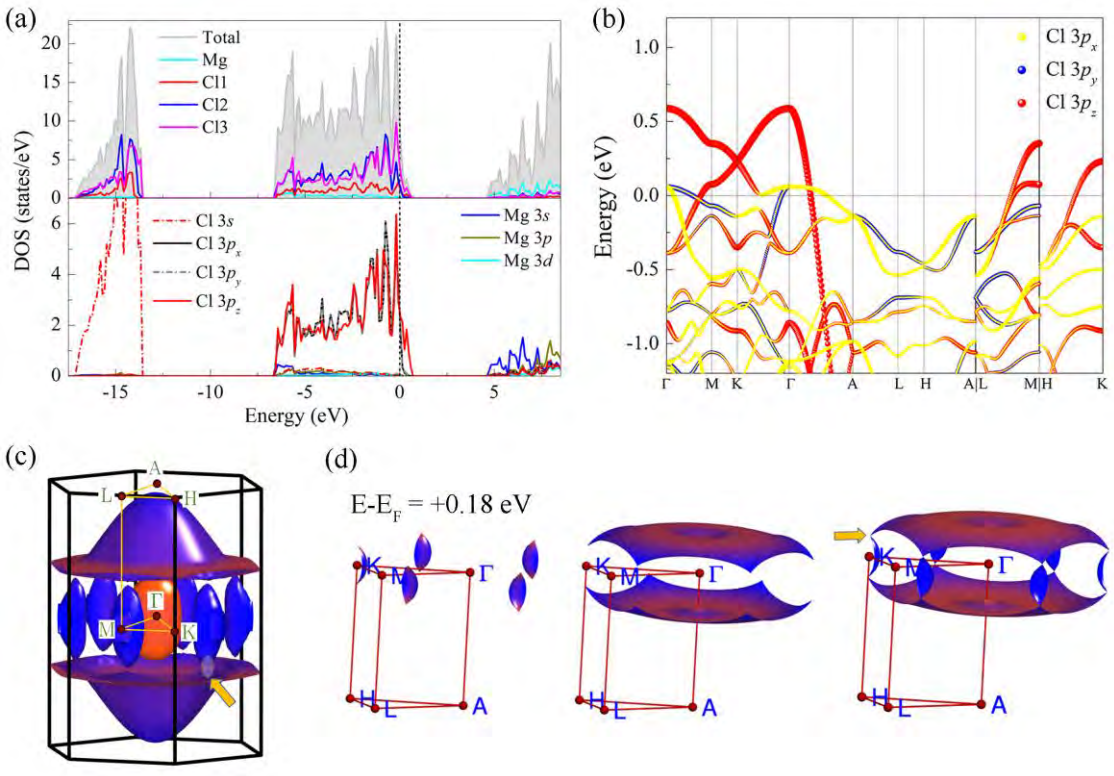

Fig. 5. Electronic properties of the Mg_3Cl_7 calculated at 40 GPa using the PBE functional. (a) TDOS and PDOS curves, (b) band structure, (c) Fermi surfaces and (d) the presence of an isolated touching point between two bands (highlighted by the yellow arrow) could be visualized using iso-energy band plotting (via Fermi surface calculation) at $E - E_F = +0.18$ eV relative to the Fermi energy. The Fermi energy level was set to 0 eV.

3.2.3. Nature of Chemical Bonding in Mg_3Cl_7

The Th_7Fe_3 structural type is well-known among polar intermetallics (La_7Ir_3[23] is an example). This structural type is also found in borides, carbides, phosphides and nitrides.[24] Typically, in Me_7X_3 (Me is an electropositive atom, X is a main group electronegative element like B, C, or N) the structure is stabilized by the metallic interactions between the Me atoms. The Me-Me distances are comparable to those in pure Me metals (see Ref.[24] for further details), with a pronounced DOS at the E_F characteristic for metallic bonding.

The structure of Mg_3Cl_7 can be described as an anti-Th_7Fe_3-type structure, as the electropositive and electronegative atoms swap their positions. To the best of our knowledge, this has not been observed so far.

To characterize the chemical bonding and the origin of unique electronic properties of the Mg_3Cl_7 compound, the electron localization function (ELF), the differential charge density distribution, Löwdin charge, crystal orbital Hamilton population (COHP),[25] crystal orbital bond index (COBI),[26] and the integrated values of the latter two (ICOHP and ICOBI), as well as the non-covalent interaction (NCI) index[27] were calculated for Mg_3Cl_7 at 40 GPa.

The ICOBI and -ICOHP values for different interatomic interactions are summarized in Table S3 (ICOBI ≈ 1 indicates strong covalent bonding, while ICOBI ≈ 0 – ionic bonding (dominant electrostatic interactions)[26]). For Mg-Cl bonds in Mg_3Cl_7 at 40 GPa, the ICOBI values are of ~0.12, suggesting primarily ionic bonding with a minor contribution of weak covalent interactions with insignificant electron sharing. The calculated -ICOHP value for purely ionic Na-Cl bonds in NaCl, where orbital overlap is mostly absent, is of ~0.56 at 50 GPa[11], whereas for the Mg-Cl bonds in Mg_3Cl_7, the -ICOHP values are just slightly higher (of ~1). Therefore, the Mg-Cl bonds in Mg_3Cl_7 can be considered as mainly ionic but display a small yet non-negligible covalent character attributed to anion polarization[28]. Interestingly, the calculated ICOBI and -ICOHP values of the Mg-Cl bonds in layered β-$MgCl_2$ [29] are found to be comparable to those in Mg_3Cl_7 (Table S3). The Löwdin charges of Mg atoms in Mg_3Cl_7 are comparable to those in β-$MgCl_2$ (1.43 vs 1.42; Table S4), but for all Cl atoms in Mg_3Cl_7 exhibit slightly lower values. Specifically, the charges for Cl1, Cl2, and Cl3 in Mg_3Cl_7 are -0.55, -0.68, and -0.57, respectively, compared to -0.71 for Cl1 in β-$MgCl_2$ (Table S4).

The calculated ELF (Fig. 6a) further reveals the polar covalent component within the (predominantly) ionic Mg-Cl interactions in Mg_3Cl_7. The shapes of the electron-rich shells localized around the Cl anions deviate from spherical and are elongated toward the neighboring Mg atoms, clearly illustrating anion polarization effects. For example, for Cl1 atoms with coordination number CN = 3, the ELF contours appear distinctly three petal-shaped (Fig. 6a).

Most importantly, the anion polarization observed in Mg_3Cl_7 leads to complex Cl-Cl interactions. At first glance, the Cl-Cl interactions in Mg_3Cl_7 exhibit ICOBI values consistent with the closed-shell interaction range (e.g. for Cl3-Cl3, ICOBI = 0.02). However, plotting of the COHP curves of all Cl-Cl distances below 3 Å reveals a shift of the antibonding states, primarily the $\sigma 3p_z^*$ associated with Cl3-Cl3 and Cl1-Cl3 interactions, towards to above E_F (Fig. S4).

This could be explained as follows: when a Cl atom forms partially covalent bonds with its neighboring Mg atoms, electron density redistribution occurs, leading the electrostatic potential anisotropy. Taking Cl1 atom in Fig. 6b for example, the coordination with three Mg atoms generates three electron deficient regions at the extensions of the Mg-Cl bonds (positions of the red arrows – noted with "δ^+" in Fig. 6). In contrast, for a Cl3 atom, which is coordinated to only two Mg atoms, two electron deficient regions form (Fig. 6b). These electron deficient regions around halogen atoms, called (or similar to) σ-hole,[30] are known to attract electron rich sites, such as lone pairs, representing a specific type of non-covalent interaction. That implies the orientation of electron deficient ("δ^+") and rich regions (noted with "δ^-") allows the σ-hole of one Cl atom to attract the lone pair of a neighboring Cl atom, forming (distorted) sigma-hole interactions. Following the principle that stronger non-covalent interactions generally correspond to shorter bond distances, the strongest attraction appears between the first-neighboring Cl atoms (that is Cl3-Cl3 interactions shown in Fig. 6c-e). These σ-hole interactions and the delocalization of electrons into the electron deficient regions result in subtle bonding effects that extend beyond purely van der Waals interactions.

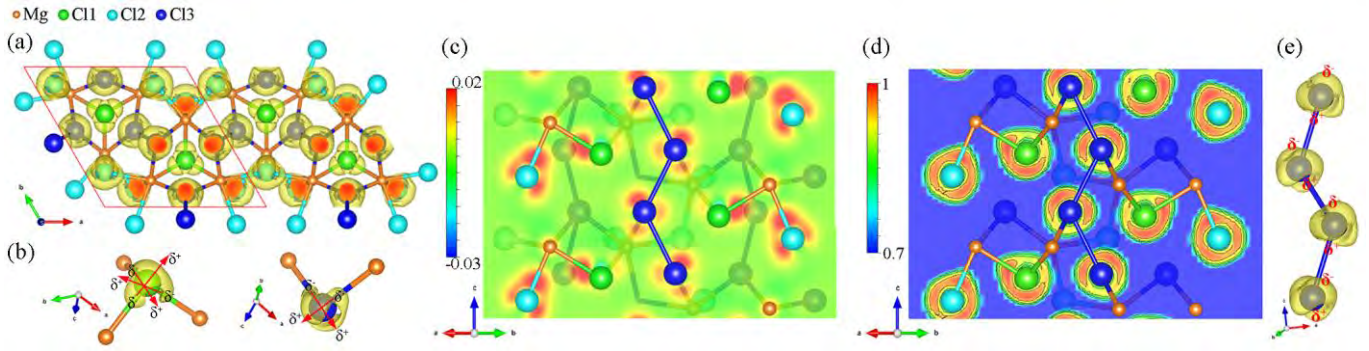

Fig. 6. (a) ELF of Mg_3Cl_7 at 40 GPa. (b) ELF highlighting electron deficient (noted with "δ^+") and rich (noted with "δ^-") regions around Cl1 and Cl3 atoms. Red arrows are guide for eyes to find the extension of the Mg-Cl bonds. (c) Differential charge density map and (d) ELF map in the (1 1 0) plane. (e) ELF showing Cl3-Cl3 interactions. The color scale in (c) is in e/Å^3. The isosurface values in (a), (b), and (e) are set as 0.85. Mg, Cl1, Cl2, and Cl3 atoms are shown in orange, green, cyan, and blue, respectively.

The above analysis is further supported by the DFT calculations of the change of electrostatic energy as a function of pressure, and as a function of the *c*/*a* ratio of Mg_3Cl_7 (Fig. S5). In the whole pressure range up to 50 GPa (Fig. S5a), the electrostatic (Madelung) energy of Mg_3Cl_7 shows continuous decrease with increasing pressure, contributing to the stabilization of its structure. This trend indicates that the attractive Cl-Cl interactions, interpreted as pressure-enhanced non-covalent interactions through the shortening of the Cl-Cl contacts, compensate for the loss in band energy[31] of Mg_3Cl_7 compared to known compounds in the Mg-Cl system, e.g. β-$MgCl_2$ which is thermodynamically stable in the comparable pressure range (see Methods). The structures relaxed with a fixed cell shape at a volume of 275.558 Å^3 (~40 GPa), revealing that a lower *c*/*a* ratio corresponds to stronger Cl3-Cl3 non-covalent interactions with shorter interatomic distances (Fig. S5b). Since halogen bonding is predominantly attractive, the electrostatic (Madelung) energy decreases continuously (becomes more negative) as the *c*/*a* ratio decreases, contributing to the stabilization of the structure (Fig. S5b). However, the band energy[31] exhibits an opposing trend with an increase of the overall band energy, which destabilizes the electronic structure (Fig. S5b). The competition between the stabilizing electrostatic energy and the destabilizing band energy defines an optimal *c*/*a* ratio where the system achieves energetic balance, aligning with the experimentally observed crystal structure. The attractive nature of halogen bonding in Mg_3Cl_7 is confirmed by the analysis of the NCI index based on the reduced density gradient (RDG) (see Methods) plotted as a function of sign(λ_2)ρ (where sign(λ_2) is the sign of the second eigenvalue of the electron density Hessian matrix).[27] As shown in Fig. S5c on the example of calculations performed at a volume of 275.558 Å^3 (~40 GPa), a prominent spike corresponding to the Cl3-Cl3 interactions is located well within the negative sign(λ_2)ρ region, demonstrating attractive interactions.[27, 32] As the density value of the spike with low RDG is related to the strength of the interaction,[32] one could notice a significant enhancement of Cl3-Cl3 interaction as the *c*/*a* ratio decreases from 0.64 to 0.58 (Fig. S5 c-e).

CONCLUSIONS

To summarize, here we synthesized a novel polar metal, magnesium chloride Mg_3Cl_7, upon laser heating of Mg in CCl_4 at pressures of 44(3), 64(3), 65(5), 73(3), 83(3), and 93(3) GPa and observed this phase upon decompression after laser heating at 28(2) GPa. The structure of the phase at each pressure point was solved and refined *in situ* using HP synchrotron SCXRD. Across the studied pressure range, Mg_3Cl_7 appears in the structure with the polar space group $P6_3mc$, which can be represented as built of interconnected triads of $MgCl_6$ prisms stacked along the polar *c* direction. To the best of our knowledge, this is the first example of an anti-Th_7Fe_3-type structure, in which electropositive and electronegative atoms have swapped positions.

Material is SHG active. Temperature-dependent resistance measurements gave evidence of the metal-like behavior of the Mg_3Cl_7 compound. Our experimental study combined with *ab initio* calculations revealed the unique combination of electronic properties (metallicity of the polar structure) and characteristics of chemical bonding of the material: the anisotropic electronic structure, the similarity of the electronic structure to that of the hole-doped semiconductors, and the attractive halogen σ-hole bonding. The synthesis of the Mg_3Cl_7 compound under HP gives evidence that pressure stabilizes unconventional polar metal materials.

METHODS

Sample preparation

Three BX90-type screw-driven diamond anvil cells (DACs)[33] equipped with 250 (DAC #1) and 120 μm (DAC #2, #3) culet diamond anvils were used. The sample chambers were formed by pre-indenting rhenium gaskets to ~30 and 20 μm thickness and laser-drilling a hole of 120 and 60 μm, depending on the culet size. DAC #1 was loaded with a piece of magnesium flake and a drop of liquid CCl_4 that acts as the chlorine source. DAC #2 was loaded with the same starting materials, but four magnesium flakes were arranged as electrodes inside the pressure chamber and connected with four platinum electrodes outside the pressure chamber for resistance measurements. DAC #3 was loaded with a piece of platinum arranged as four electrodes in CCl_4 (act as a pressure medium. The experiment in DAC #3 aimed at comparing the resistance of a known metal Pt with the resistance of Mg_3Cl_7 measured in DAC #2 at similar PT conditions. Resistance measurements were performed in van der Pauw geometry upon sample warming from ~80 K to room temperature using GOM-804 Milli-Ohm Meter (Good Will Instrument Co., Ltd.). The pressure was measured *in situ* using the equation of state of rhenium.[34] Double-sided laser-heating of the samples up to ~2200 K was performed for DAC #1 and DAC #2 at the laboratory at the Bayerisches Geoinstitut[35] with magnesium employed as the laser light absorber. Detailed information on experimental conditions and the reaction products is summarized in Table S1.

X-ray diffraction

Synchrotron X-ray diffraction measurements of the compressed samples were performed at ID11 (λ = 0.2844 Å, beam size ~ 0.75 × 0.75 μm^2), ID15b (λ = 0.4100 Å, beam size ~ 1.5 × 1.5 μm^2), and ID27 (λ = 0.3738 Å, beam size ~ 1.5 × 1.5 μm^2) of the EBS-ESRF, and the P02.2 beamline (λ = 0.2910 Å, beam size ~2.0 × 2.0 μm^2) of PETRA III. In order to determine the sample position for single-crystal X-ray diffraction data acquisition, a full X-ray diffraction mapping of the pressure chamber was performed. The sample positions displaying the greatest number of single-crystal reflections belonging to the phases of interest were chosen, and step-scans of 0.5° from −36° to +36° ω were performed. The CrysAlis^{Pro} software[36] was utilized for the single-crystal data analysis. To calibrate the instrumental model in the CrysAlis^{Pro} software, *i.e.* the sample-to-detector distance, detector's origin, offsets of the goniometer angles, and rotation of both the X-ray beam and detector around the instrument axis, we used a single crystal of vanadinite [$Pb_5(VO_4)_3Cl$, $P6_3/m$ space group, a = 10.3174(30) Å, and c = 7.3378(30) Å] at ID15b, and orthoenstatite [$(Mg_{1.93}Fe_{0.06})(Si_{1.93}Al_{0.06})O_6$, *Pbca* space group, a = 8.8117(2) Å, b = 5.1832(10) Å, and c = 18.2391(3) Å] at the other beamlines. The DAFi program[14] was used for the search of reflections' groups belonging to individual single-crystal domains. The crystal structures were then solved and refined using the OLEX2[37] software. The crystallite sizes were estimated from X-ray maps using the XDI software.[38] The crystallographic information is available in Tables S2.

Density functional theory calculations

First-principles calculations were performed in the framework of density functional theory (DFT) as implemented in the Vienna Ab initio Simulation Package (VASP)[39] using the Projector-Augmented-Wave (PAW) method[40-41], and the all-electron, full-potential code FHI-aims using the linear combination of numeric

atom-centered orbitals (NAOs) method.[42-44] The Generalized Gradient Approximation (GGA) functional is used for calculating the exchange-correlation energies, as proposed by Perdew–Burke–Ernzerhof (PBE).[45] Additional calculations for the band structures were performed with the Heyd-Scuseria-Ernzerhof (HSE) hybrid functional.[46] The PAW potentials adapted from the VASP library with the following valence configurations of 3*s* for Mg, 3*s*3*p* for Cl, 2*s*2*p* for O, and 1*s* for H were used with the Mg, Cl, O, and H_h POTCARs. The plane-wave kinetic energy cutoff was set to 600 eV. Van der Waals interactions were captured with the use of the vdW-optB88 functional[47-48]. We performed variable cell relaxations including lattice parameters and atomic positions on the synthesized experimental structure to optimize the atomic coordinates and the cell vectors until the total forces were smaller than 10^{-3} eV $Å^{-1}$ per atom using the conjugate-gradient (CG) algorithm. In geometry optimization, we used a Γ-centred k-mesh of 13x11x11 (for Mg(OH)Cl), and 7x7x11 (for Mg_3Cl_7), respectively. To increase the accuracy of ground-state electron density and density of states (DOS), a denser Γ-centred k-mesh of 19x15x15 in case of Mg(OH)Cl and 11x11x17 for Mg_3Cl_7 were used. The tetrahedron smearing method with Blöchl corrections (ISMEAR = -5) was used for the DOS and the spatial distribution of electronic density. For additional band structure calculations using FHI-aims, the default suggestions for Light Atomic Species were employed, as they produced results comparable to those obtained with VASP. We used the VASPKIT code for post-processing of the VASP calculated data.[49] The crystal structure, ELF, and charge density difference visualisation were made with the VESTA software[50]. For the convex hull calculations, the following reference phases were considered: *hcp*-Mg was taken as the stable phase at 0 and 50 GPa, while *bcc*-Mg was used at 100 GPa.[17] For elemental chlorine, the *Cmca* phase was adopted throughout the studied pressure range (0-100 GPa), as reported in Ref [18]. For $MgCl_2$, the α-$MgCl_2$ structure is the stable phase from 0 to 0.7 GPa,[15] β-$MgCl_2$ from 0.7 to 49 GPa, *oP*72-$MgCl_2$ from 49 to 52 GPa, and *oP*12-$MgCl_2$ from 52 to 100 GPa. The density-functional-perturbation theory (DFPT) (for Mg(OH)Cl), and the finite displacement method (for Mg_3Cl_7), as implemented in PHONOPY[51], were used to calculate harmonic phonon frequencies and phonon band structures. A supercell size of 2x2x2 in case of Mg(OH)Cl, and 2x2x3 for Mg_3Cl_7 were used with k-mesh size of 2x2x2 in all cases were used for the harmonic phonon calculations at 0 K. Löwdin charge, crystal orbital Hamilton population (COHP), and crystal orbital bond index (COBI) analyses were performed using the LOBSTER package.[25-26, 52-54] Non-covalent interaction (NCI)[27] plots were computed with the Critic2 code,[32, 55-56] compatible with VASP output files. The reduced density gradient (RDG) is expressed as $RDG = \frac{|\nabla\rho|}{2(3\pi^2)^{1/3}\rho^{4/3}}$.[27] The Fermi surface and plasmon frequencies were calculated using the Full Potential Local Orbital (FPLO) code[57] with the tetrahedron method and high density k-mesh subdivision. To expose the topological points in the electronic structure the band structure has been wannierized using symmetry-conserving maximally projected Wannier functions (see Supplementary Discussion 2).[58]

ACKNOWLEDGMENTS

The authors acknowledge the Deutsches Elektronen-Synchrotron (DESY, PETRA III) and the European Synchrotron Radiation Facility (ESRF) for the provision of beamtime at the P02.2, and ID11, ID15b and ID27 beamlines, respectively. Y.Y. acknowledges insightful discussions with Prof. Sergey Simak (IFM, Linköping University) regarding the calculations of electrostatic and band energy of Mg_3Cl_7. Y.Y. and I.A.A are supported by the Knut and Alice Wallenberg Foundation (Wallenberg Scholar grant no. KAW-2018.0194). I.A.A acknowledges support by the Swedish Research Council (VR) Grant No. 2023-05358. N.D. and I.A.A. also thank the Swedish Government Strategic Research Area in Materials Science on Functional Materials at Linkoping University (Faculty Grant SFO-Mat-LiU No. 2009 00971). N.D. thanks the Deutsche Forschungsgemeinschaft (DFG; projects DU 945–15/1) for financial support. F.K. acknowledges support from

the Swedish Research Council (VR) program 2020-04630 and the Swedish e-Science Research Centre (SeRC). D.L. thanks the UKRI Future Leaders Fellowship (MR/V025724/1) for financial support. Computations were enabled by resources provided by the National Academic Infrastructure for Supercomputing in Sweden (NAISS) using Tetralith at the National Supercomputer Centre, Linkoping University.

Conflicts of Interest

The authors declare no conflicts of interest.

REFERENCES

1. Bhowal, S.; Spaldin, N. A., Polar Metals: Principles and Prospects. *Annu. Rev. Mater. Res.* **2023,** *53* (1), 53-79.
2. Anderson, P. W.; Blount, E. I., Symmetry Considerations on Martensitic Transformations: "Ferroelectric" Metals? *Phys. Rev. Lett.* **1965,** *14* (7), 217-219.
3. Shi, Y.; Guo, Y.; Wang, X.; Princep, A. J.; Khalyavin, D.; Manuel, P.; Michiue, Y.; Sato, A.; Tsuda, K.; Yu, S.; Arai, M.; Shirako, Y.; Akaogi, M.; Wang, N.; Yamaura, K.; Boothroyd, A. T., A ferroelectric-like structural transition in a metal. *Nat Mater* **2013,** *12* (11), 1024-7.
4. Kim, T. H.; Puggioni, D.; Yuan, Y.; Xie, L.; Zhou, H.; Campbell, N.; Ryan, P. J.; Choi, Y.; Kim, J. W.; Patzner, J. R.; Ryu, S.; Podkaminer, J. P.; Irwin, J.; Ma, Y.; Fennie, C. J.; Rzchowski, M. S.; Pan, X. Q.; Gopalan, V.; Rondinelli, J. M.; Eom, C. B., Polar metals by geometric design. *Nature* **2016,** *533* (7601), 68-72.
5. Zhang, J.; Shen, S.; Puggioni, D.; Wang, M.; Sha, H.; Xu, X.; Lyu, Y.; Peng, H.; Xing, W.; Walters, L. N.; Liu, L.; Wang, Y.; Hou, D.; Xi, C.; Pi, L.; Ishizuka, H.; Kotani, Y.; Kimata, M.; Nojiri, H.; Nakamura, T.; Liang, T.; Yi, D.; Nan, T.; Zang, J.; Sheng, Z.; He, Q.; Zhou, S.; Nagaosa, N.; Nan, C. W.; Tokura, Y.; Yu, R.; Rondinelli, J. M.; Yu, P., A correlated ferromagnetic polar metal by design. *Nat Mater* **2024,** *23* (7), 912-919.
6. Puggioni, D.; Rondinelli, J. M., Designing a robustly metallic noncenstrosymmetric ruthenate oxide with large thermopower anisotropy. *Nat Commun* **2014,** *5*, 3432.
7. Wang, Y.; Li, D.; Duan, S.; Sun, S.; Ding, Y.; Bussolotti, F.; Sun, M.; Chen, M.; Wang, M.; Chen, L.; Wu, K.; Goh, K. E. J.; Wee, A. T. S.; Zhou, M.; Feng, B.; Hua, C.; Huang, Y. L.; Chen, W., Realization of Two-dimensional Intrinsic Polar metal in a Buckled Honeycomb Binary Lattice. *Adv. Mater.* **2024**, e2404341.
8. Fei, Z.; Zhao, W.; Palomaki, T. A.; Sun, B.; Miller, M. K.; Zhao, Z.; Yan, J.; Xu, X.; Cobden, D. H., Ferroelectric switching of a two-dimensional metal. *Nature* **2018,** *560* (7718), 336-339.
9. Sharma, P.; Xiang, F.-X.; Shao, D.-F.; Zhang, D.; Tsymbal, E. Y.; Hamilton, A. R.; Seidel, J., A room-temperature ferroelectric semimetal. *Sci Adv* **2019,** *5* (7), eaax5080.
10. Benedek, N. A.; Birol, T., 'Ferroelectric' metals reexamined: fundamental mechanisms and design considerations for new materials. *J. Mater. Chem. C* **2016,** *4* (18), 4000-4015.
11. Yin, Y.; Aslandukova, A.; Jena, N.; Trybel, F.; Abrikosov, I. A.; Winkler, B.; Khandarkhaeva, S.; Fedotenko, T.; Bykova, E.; Laniel, D.; Bykov, M.; Aslandukov, A.; Akbar, F. I.; Glazyrin, K.; Garbarino, G.; Giacobbe, C.; Bright, E. L.; Jia, Z.; Dubrovinsky, L.; Dubrovinskaia, N., Unraveling the Bonding Complexity of Polyhalogen Anions: High-Pressure Synthesis of Unpredicted Sodium Chlorides Na(2)Cl(3) and Na(4)Cl(5) and Bromide Na(4)Br(5). *JACS Au* **2023,** *3* (6), 1634-1641.
12. Poreba, T.; Racioppi, S.; Garbarino, G.; Morgenroth, W.; Mezouar, M., Investigating the Structural Symmetrization of CsI3 at High Pressures through Combined X-ray Diffraction Experiments and Theoretical Analysis. *Inorg. Chem.* **2022,** *61*, 10977.
13. Cavallo, G.; Metrangolo, P.; Milani, R.; Pilati, T.; Priimagi, A.; Resnati, G.; Terraneo, G., The Halogen Bond. *Chem. Rev.* **2016,** *116* (4), 2478-601.
14. Aslandukov, A.; Aslandukov, M.; Dubrovinskaia, N.; Dubrovinsky, L., Domain Auto Finder (DAFi) program: the analysis of single-crystal X-ray diffraction data from polycrystalline samples. *J. Appl. Crystallogr.* **2022,** *55* (Pt 5), 1383-1391.
15. Stavrou, E.; Yao, Y.; Zaug, J. M.; Bastea, S.; Kalkan, B.; Konopkova, Z.; Kunz, M., High-pressure X-ray diffraction, Raman, and computational studies of MgCl2 up to 1 Mbar: Extensive pressure stability of the beta-MgCl2 layered structure. *Sci Rep* **2016,** *6*, 30631.
16. Sun, W.; Dacek, S. T.; Ong, S. P.; Hautier, G.; Jain, A.; Richards, W. D.; Gamst, A. C.; Persson, K. A.; Ceder, G., The thermodynamic scale of inorganic crystalline metastability. *Sci Adv* **2016,** *2* (11), e1600225.
17. Olijnyk, H.; Holzapfel, W. B., High-pressure structural phase transition in Mg. *Phys Rev B Condens Matter* **1985,** *31* (7), 4682-4683.
18. Dalladay-Simpson, P.; Binns, J.; Pena-Alvarez, M.; Donnelly, M. E.; Greenberg, E.; Prakapenka, V.; Chen,

X. J.; Gregoryanz, E.; Howie, R. T., Band gap closure, incommensurability and molecular dissociation of dense chlorine. *Nat. Commun.* **2019,** *10* (1), 1134.
19. Laniel, D.; Winkler, B.; Fedotenko, T.; Aslandukova, A.; Aslandukov, A.; Vogel, S.; Meier, T.; Bykov, M.; Chariton, S.; Glazyrin, K.; Milman, V.; Prakapenka, V.; Schnick, W.; Dubrovinsky, L.; Dubrovinskaia, N., High-pressure Na3(N2)4, Ca3(N2)4, Sr3(N2)4, and Ba(N2)3 featuring nitrogen dimers with noninteger charges and anion-driven metallicity. *Phys. Rev. Mater.* **2022,** *6* (2), 023402.
20. Aslandukov, A.; Trybel, F.; Aslandukova, A.; Laniel, D.; Fedotenko, T.; Khandarkhaeva, S.; Aprilis, G.; Giacobbe, C.; Lawrence Bright, E.; Abrikosov, I. A.; Dubrovinsky, L.; Dubrovinskaia, N., Anionic N(18) Macrocycles and a Polynitrogen Double Helix in Novel Yttrium Polynitrides YN(6) and Y(2) N(11) at 100 GPa. *Angew. Chem. Int. Ed. Engl.* **2022,** *61* (34), e202207469.
21. Bhattacharyya, G.; Choudhuri, I.; Bhauriyal, P.; Garg, P.; Pathak, B., Ferromagnetism in magnesium chloride monolayer with an unusually large spin-up gap. *Nanoscale* **2018,** *10* (47), 22280-22292.
22. Gao, H.; Kim, Y.; Venderbos, J. W. F.; Kane, C. L.; Mele, E. J.; Rappe, A. M.; Ren, W., Dirac-Weyl Semimetal: Coexistence of Dirac and Weyl Fermions in Polar Hexagonal ABC Crystals. *Phys. Rev. Lett.* **2018,** *121* (10), 106404.
23. Barker, J. A.; Singh, D.; Thamizhavel, A.; Hillier, A. D.; Lees, M. R.; Balakrishnan, G.; Paul, D. M.; Singh, R. P., Unconventional Superconductivity in La(7)Ir(3) Revealed by Muon Spin Relaxation: Introducing a New Family of Noncentrosymmetric Superconductor That Breaks Time-Reversal Symmetry. *Phys. Rev. Lett.* **2015,** *115* (26), 267001.
24. Dubrovinsky, L.; Khandarkhaeva, S.; Fedotenko, T.; Laniel, D.; Bykov, M.; Giacobbe, C.; Lawrence Bright, E.; Sedmak, P.; Chariton, S.; Prakapenka, V.; Ponomareva, A. V.; Smirnova, E. A.; Belov, M. P.; Tasnádi, F.; Shulumba, N.; Trybel, F.; Abrikosov, I. A.; Dubrovinskaia, N., Materials synthesis at terapascal static pressures. *Nature* **2022,** *605* (7909), 274-278.
25. Dronskowski, R.; Bloechl, P. E., Crystal orbital Hamilton populations (COHP): energy-resolved visualization of chemical bonding in solids based on density-functional calculations. *J. Phys. Chem.* **2002,** *97* (33), 8617-8624.
26. Müller, P. C.; Ertural, C.; Hempelmann, J.; Dronskowski, R., Crystal Orbital Bond Index: Covalent Bond Orders in Solids. *J Phys Chem C* **2021,** *125* (14), 7959-7970.
27. Johnson, E. R.; Keinan, S.; Mori-Sanchez, P.; Contreras-Garcia, J.; Cohen, A. J.; Yang, W., Revealing noncovalent interactions. *J. Am. Chem. Soc.* **2010,** *132* (18), 6498-506.
28. Taylor, M. S., Anion recognition based on halogen, chalcogen, pnictogen and tetrel bonding. *Coord. Chem. Rev.* **2020,** *413*.
29. Wilson, M.; Madden, P. A., Anion polarization and the stability of layered structures in MX2systems. *J. Phys.: Condens. Matter* **1994,** *6* (1), 159-170.
30. Lim, J. Y. C.; Beer, P. D., Sigma-Hole Interactions in Anion Recognition. *Chem* **2018,** *4* (4), 731-783.
31. Häussermann, U.; Simak, S. I.; Ahuja, R.; Johansson, B., A Unified Bonding Picture for the Metallic Triel Elements. *Angew. Chem. Int. Ed.* **2000,** *39* (7), 1246-1249.
32. Otero-de-la-Roza, A.; Johnson, E. R.; Contreras-Garcia, J., Revealing non-covalent interactions in solids: NCI plots revisited. *Phys. Chem. Chem. Phys.* **2012,** *14* (35), 12165-72.
33. Kantor, I.; Prakapenka, V.; Kantor, A.; Dera, P.; Kurnosov, A.; Sinogeikin, S.; Dubrovinskaia, N.; Dubrovinsky, L., BX90: a new diamond anvil cell design for X-ray diffraction and optical measurements. *Rev. Sci. Instrum.* **2012,** *83* (12), 125102.
34. Anzellini, S.; Dewaele, A.; Occelli, F.; Loubeyre, P.; Mezouar, M., Equation of state of rhenium and application for ultra high pressure calibration. *J. Appl. Phys.* **2014,** *115* (4).
35. Fedotenko, T.; Dubrovinsky, L.; Aprilis, G.; Koemets, E.; Snigirev, A.; Snigireva, I.; Barannikov, A.; Ershov, P.; Cova, F.; Hanfland, M., Laser heating setup for diamond anvil cells for in situ synchrotron and in house high and ultra-high pressure studies. *Rev. Sci. Instrum.* **2019,** *90* (10), 104501.
36. Rigaku Oxford Diffraction Ltd. In *Rigaku OD and CryAlis PRO*, 2018.
37. Dolomanov, O. V.; Bourhis, L. J.; Gildea, R. J.; Howard, J. A. K.; Puschmann, H., OLEX2: a complete

structure solution, refinement and analysis program. *J. Appl. Crystallogr.* **2009,** *42* (2), 339-341.
38. Hrubiak, R.; Smith, J. S.; Shen, G., Multimode scanning X-ray diffraction microscopy for diamond anvil cell experiments. *Rev. Sci. Instrum.* **2019,** *90* (2), 025109.
39. Kresse, G.; Furthmuller, J., Efficiency of ab-initio total energy calculations for metals and semiconductors using a plane-wave basis set. *Comput. Mater. Sci.* **1996,** *6* (1), 15-50.
40. Blochl, P. E., Projector augmented-wave method. *Phys Rev B* **1994,** *50* (24), 17953-17979.
41. Kresse, G.; Joubert, D., From ultrasoft pseudopotentials to the projector augmented-wave method. *Phys Rev B* **1999,** *59* (3), 1758-1775.
42. Blum, V.; Rossi, M.; Kokott, S.; Scheffler, M., The FHI-aims Code: All-electron, ab initio materials simulations towards the exascale. *arXiv preprint* **2022**, 12335.
43. Blum, V.; Gehrke, R.; Hanke, F.; Havu, P.; Havu, V.; Ren, X.; Reuter, K.; Scheffler, M., Ab initio molecular simulations with numeric atom-centered orbitals. *Comput. Phys. Commun.* **2009,** *180* (11), 2175-2196.
44. Ren, X.; Rinke, P.; Blum, V.; Wieferink, J.; Tkatchenko, A.; Sanfilippo, A.; Reuter, K.; Scheffler, M., Resolution-of-identity approach to Hartree–Fock, hybrid density functionals, RPA, MP2 and GW with numeric atom-centered orbital basis functions. *New J. Phys.* **2012,** *14* (5).
45. Perdew, J. P.; Burke, K.; Ernzerhof, M., Generalized Gradient Approximation Made Simple. *Phys. Rev. Lett.* **1996,** *77* (18), 3865-3868.
46. Heyd, J.; Scuseria, G. E.; Ernzerhof, M., Hybrid functionals based on a screened Coulomb potential. *J. Chem. Phys.* **2003,** *118* (18), 8207-8215.
47. Klimeš, J.; Bowler, D. R.; Michaelides, A., Van der Waals density functionals applied to solids. *Phys Rev B* **2011,** *83* (19), 195131.
48. Klimeš, J.; Bowler, D. R.; Michaelides, A., Chemical accuracy for the van der Waals density functional. *J. Phys.: Condens. Matter* **2009,** *22* (2), 022201.
49. Wang, V.; Xu, N.; Liu, J.-C.; Tang, G.; Geng, W.-T., VASPKIT: A user-friendly interface facilitating high-throughput computing and analysis using VASP code. *Comput. Phys. Commun.* **2021,** *267*.
50. Momma, K.; Izumi, F., VESTA: a three-dimensional visualization system for electronic and structural analysis. *J. Appl. Crystallogr.* **2008,** *41* (3), 653-658.
51. Togo, A.; Oba, F.; Tanaka, I., First-principles calculations of the ferroelastic transition between rutile-type and CaCl2-type SiO2 at high pressures. *Phys Rev B* **2008,** *78* (13), 134106.
52. Deringer, V. L.; Tchougreeff, A. L.; Dronskowski, R., Crystal orbital Hamilton population (COHP) analysis as projected from plane-wave basis sets. *J. Phys. Chem. A* **2011,** *115* (21), 5461-6.
53. Maintz, S.; Deringer, V. L.; Tchougreeff, A. L.; Dronskowski, R., Analytic projection from plane-wave and PAW wavefunctions and application to chemical-bonding analysis in solids. *J. Comput. Chem.* **2013,** *34* (29), 2557-67.
54. Maintz, S.; Deringer, V. L.; Tchougreeff, A. L.; Dronskowski, R., LOBSTER: A tool to extract chemical bonding from plane-wave based DFT. *J. Comput. Chem.* **2016,** *37* (11), 1030-5.
55. Otero-de-la-Roza, A.; Blanco, M. A.; Pendás, A. M.; Luaña, V., Critic: a new program for the topological analysis of solid-state electron densities. *Comput. Phys. Commun.* **2009,** *180* (1), 157-166.
56. Otero-de-la-Roza, A.; Johnson, E. R.; Luaña, V., Critic2: A program for real-space analysis of quantum chemical interactions in solids. *Comput. Phys. Commun.* **2014,** *185* (3), 1007-1018.
57. Koepernik, K.; Eschrig, H., Full-potential nonorthogonal local-orbital minimum-basis band-structure scheme. *Physical Review B* **1999,** *59* (3), 1743.
58. Koepernik, K.; Janson, O.; Sun, Y.; Van Den Brink, J., Symmetry-conserving maximally projected Wannier functions. *Physical Review B* **2023,** *107* (23), 235135.